Journal of Magnetic Resonance 207 (2010) 69–77

Contents lists available at ScienceDirect

Journal of Magnetic Resonance

journal homepage: www.elsevier.com/locate/jmr

In vivo multisite oximetry using EPR–NMR coimaging

R. Ahmad [a,*], G. Caia [a], L.C. Potter [b], S. Petryakov [a], P. Kuppusamy [a], J.L. Zweier [a,**]

[a] Center for Biomedical EPR Spectroscopy and Imaging, Davis Heart and Lung Research Institute, Department of Internal Medicine, The Ohio State University, Columbus, OH 43210, USA
[b] Department of Electrical and Computer Engineering, The Ohio State University, Columbus, OH 43210, USA

ARTICLE INFO

Article history:
Received 1 February 2010
Revised 19 May 2010
Available online 24 August 2010

Keywords:
EPR
EPRI
MRI
Coimaging
Oximetry
Multisite

ABSTRACT

Coimaging employing electron paramagnetic resonance (EPR) imaging and MRI is used for rapid *in vivo* oximetry conducted simultaneously across multiple organs of a mouse. A recently developed hybrid EPR–NMR coimaging instrument is used for both EPR and NMR measurements. Oxygen sensitive particulate EPR probe is implanted in small localized pockets, called sites, across multiple regions of a live mouse. Three dimensional MRI is used to generate anatomic visualization, providing precise locations of implant sites. The pO_2 values, one for every site, are then estimated from EPR measurements. To account for radio frequency (RF) phase inhomogeneities inside a large resonator carrying a lossy sample, a generalization of an existing EPR data model is proposed. Utilization of known spectral lineshape, sparse distribution, and known site locations reduce the EPR data collection by more than an order of magnitude over a conventional spectral–spatial imaging, enhancing the feasibility of *in vivo* EPR oximetry for clinically relevant models.

1. Introduction

Existing literature [1,2] builds a compelling case for the critical role of oxygen in the evolution of life on earth. Aerobic organisms consume molecular oxygen (O_2) to generate chemical energy, required for biologic processes, in the form of adenosine triphosphate. Also, O_2 serves as a regulatory molecule for important physiologic processes. Hence, a precise knowledge of the levels of oxygen in tissues of interest is of great importance in understanding normal physiology as well as the pathogenesis of disease. Several techniques [3,4], including electron paramagnetic resonance (EPR) spectroscopy and imaging (EPRI) [5], have been employed for oxygen measurements in biological samples.

1.1. EPR oximetry

Measurement of oxygen concentration by EPR (EPR oximetry) [6–9] involves the use of an exogenous spin probe consisting of paramagnetic material in either particulate or soluble form. Changes in the EPR spectral width (linewidth) are caused by the interaction of two paramagnetic species – molecular oxygen and the spin probe. This interaction-induced reversible line broadening quantifies oxygen levels. EPR oximetry possesses a high sensitivity to molecular oxygen and is capable of measuring direct and absolute values of pO_2 or O_2 concentration. It can further provide three dimensional mapping of oxygen distribution, if required. This method generally shows a high specificity because of minimal interference from other sources. In addition, a number of developed EPR probes are nontoxic, and are generally stable in a tissue environment. In fact, particulate EPR probes can stay in a biological sample for months [10] without losing their oxygen sensitivity. Therefore, particulate-based EPR oximetry is usually described as 'minimally invasive' as only one-time implantation is needed, and the subsequent measurements are carried out without further invasive procedures. The biological applications for EPR oximetry have been rapidly growing [11] and include measuring tumor oxygenation for determining cancer treatment efficacy [12] and measuring tissue oxygen for estimating the extent of myocardial injury during both ischemia and subsequent reperfusion [13,14].

For EPR-based oximetry, there are two modes of data collection: spectroscopy and spectral–spatial imaging. In spectroscopic mode, the EPR spectrum, also called lineshape, is observed by measuring the absorption of monochromatic radiation in the presence of an external magnetic field. Since there are no magnetic gradients or other means of spatial encoding, the spectroscopy does not provide spin density distributions. Also, this mode is generally not suitable for samples with spatially varying lineshapes because the measured spectrum is a sum of spectra from all irradiated sample locations. In spectral–spatial mode [15], a spectral dimension, in addition to one or more spatial dimensions, is required to capture the lineshape information. The spatial and spectral information is

* Corresponding author. Address: 420 W. 12th Avenue, Suite 126A, Columbus, OH 43210, USA. Fax: +1 614 292 8454.
** Corresponding author. Address: 473 W. 12th Avenue, Suite 110, Columbus, OH 43210, USA. Fax: +1 614 247 7845.
E-mail addresses: rizwan.ahmad@osumc.edu (R. Ahmad), jay.zweier@osumc.edu (J.L. Zweier).

1090-7807/$ - see front matter © 2010 Elsevier Inc. All rights reserved.
doi:10.1016/j.jmr.2010.08.011

encoded by collecting data under various magnetic field gradient orientations and strengths. Using spectral–spatial imaging, one can extract both spin density and pO_2 distributions simultaneously. For a setup with high signal-to-noise ratio (SNR), the data acquisitions based on fast scan [16] or spinning gradient [17] can provide substantial acceleration over the conventional slow scan-based acquisition. For low SNR, however, the spectral–spatial imaging, especially when performed over three spatial dimensions, remains a time consuming proposition. In addition to suffering from long data collection times, EPR spectral–spatial imaging also lacks the capability of providing anatomic details of the subject.

Several innovations, ranging from improved hardware designs to optimized data collection and processing schemes, have been proposed and implemented to reduce the data collection time to the levels suitable for *in vivo* studies. For instance, rapid scan [18], parametric reconstruction [19], overmodulation [20], digital detection [21], and pulsed-EPR [22] have been developed and used to either improve SNR or reduce the data acquisition times. The proposed postprocessing approach for multisite oximetry can work in conjunction with any data collection modality as long as the data can be represented in the form of conventional slow scan projections.

1.2. Multisite oximetry

In 1993, Smirnov et al. [23] suggested a method of collecting oxygen information from multiple sites simultaneously, without performing the time consuming spectral–spatial imaging. The method relies on applying a magnetic gradient large enough to separate the spectra from different sites but small enough to introduce minimal distortion in the spectrum from each site. Strict constraints on the minimum separation of the sites and the magnitude of maximum gradient limit its broad application. Later, Grinberg et al. [24] suggested an improved method. By collecting two (or more) projections along a suitable gradient orientation, each with a different gradient strength, the pO_2 values at multiple sites are estimated using a convolution-based fitting method. This approach has been applied to study cerebral ischemia in rats [25]. The method relies on identifying and collecting the projections where signals from various sites minimally overlap and can be visually separated. The requirements of well-organized probe distribution, however, may become stringent for many EPR applications where the distribution cannot be confined to few well-separated spots or the user does not have a precise control or knowledge of the probe distribution. Also, its application is strictly limited to the Lorentzian lineshape.

Subsequently, Som et al. [26] suggested a more comprehensive framework for multisite oximetry. The key assumptions made are: (i) the EPR spectrum belongs to a known parametric function family; (ii) the probe distribution is spatially sparse, i.e., the localized spin pockets, called sites, constitute only a small fraction of the field-of-view (FOV); (iii) and each site exhibits a single pO_2 value. Under these assumptions, each spatial voxel is characterized by an unknown spin density and linewidth, and the proposed forward model relates the collected projection data to these unknowns. These parameters are then estimated jointly from a small set of projections.

The proposed multisite oximetry approach, which is adapted from the previously proposed method by Som et al., is more generalized in terms of accommodating an unknown nonuniform RF phase across the FOV. Also, it is less restrictive than the previous approaches [23,24]. For instance, the current approach does not impose any restrictions on the geometry or number of sites. It also does not require a priori knowledge of site locations or the most suitable gradient angle for a given geometry of sites. However, like other inverse problems, the proposed method requires an adequate number of independent measurements to reliably solve for the unknown parameters, which grow with the number and size of probe implants. The simulation results presented here also point to the applicability of this approach for random and unknown geometries with relatively large number of sites. Such a configuration would make a difficult candidate for other approaches which rely on collecting projections with visual separation and minimum overlap of signals from different sites. The current approach is a supplement and not a direct alternative to the previous methods which are more restrictive but, when applicable, can offer larger accelerations.

1.3. EPR–NMR coimaging

Several noninvasive NMR-based methods for *in vivo* detection and mapping of paramagnetic substances are under development. Both contrast-enhanced MRI [27] and proton electron double resonance imaging (PEDRI) [28] utilize NMR-based detection and therefore automatically provide coregistration of free radical distribution with anatomical structure. The availability of anatomic information, as well as superior spatial and temporal resolutions, make MRI-based techniques more efficient in these aspects compared to direct EPR methods. However, since these techniques are based on spin exchange relaxation or saturation transfer from electron spins to water protons, they are inherently indirect. Furthermore, their application is more suitable for water-soluble paramagnetic substances with small linewidths, and typically high concentrations (>1 mM) are required for optimal image contrast or enhancement. The EPR, on the other hand, has been shown to be much more versatile, enabling imaging of a broad range of soluble and particulate probes with EPR linewidths from 0.002 to 1 mT.

Recently, EPR–NMR coimaging has been developed to combine the sensitivity and directness of EPR oximetry with high-resolution anatomic visualization capability of MRI. In comparison to EPRI or MRI alone, the EPR–NMR coimaging can provide more comprehensive information. In our earlier study [29] that first reported the EPR–NMR coimaging, the data were collected on two separate EPRI and MRI instruments. Subsequently, Matsumoto et al. [30] reported coimaging of mice with EPRI imaging at 300 MHz (10.8 mT) and proton MRI at 8.5 MHz (200 mT) using a composite resonator assembly in which the sample was moved between the two different magnet systems by means of a sliding mechanism. In 2007, Kawada et al. [31] reported a novel multicoil parallel-gap design for a composite EPR–NMR resonator. Later, we reported [32] a coimaging system that utilizes a single set of field gradients and resistive magnet for both the EPRI and MRI measurements. The design of the resonator assembly holds the sample in place and allows either resonator to slide over the sample, eliminating the requirement for spatial markers and image postprocessing to achieve coregistration. More recently, the EPR–NMR coimaging has been used to study tumor oxygenation [33,34].

In this work, a synergistic relationship between EPRI and MRI for *in vivo* multisite oximetry is demonstrated. Here, MRI not only provides the anatomic details of the object but also complements the EPR oximetry by providing precise locations of particulate probe implants. In comparison to EPRI, the higher resolution of MRI allows for a selection of more compact regions around the sites, leading to a smaller number of unknowns. These unknowns, including linewidth, are then estimated from a small number of EPR projections. The remainder of the paper is organized as follows: Section 2 describes the problem formulation, instrumentation, animal model, and data collection protocol; Section 3 discusses simulation and *in vivo* oximetry results; Section 4 includes discussion; Section 5 summarizes the conclusions; and Appendix A provides the derivation of the EPR data model used in this research.

2. Materials and methods

2.1. Problem formulation

Here, we consider a more generalized EPRI data model than what has been reported previously [26]. Similar to the previous model, we assume that lineshape is a known parametric function and linewidth across each site is constant. But unlike the previous model, we also assume that RF phase is inhomogeneous [35] and varies gradually within the FOV. Therefore, we assign an unknown RF phase to each site, which implies that all voxels at each site have an identical unknown RF phase. All these unknowns, including spin density, linewidth and RF phase, are estimated jointly. The derivation of the forward model used here is given in Appendix A. The concept of multisite oximetry is captured in Fig. 1.

One noticeable improvement of the current forward model, over the previous model [26], is the inclusion of inhomogeneous RF phase. Imaging of the whole body of mouse prompts the use of large resonators and large FOVs, which, for a lossy sample, results in significant RF phase variations within the FOV. This spatial inhomogeneity of RF phase results in a signal, from each voxel, that is not purely absorption but rather a mixture of absorption and dispersion. Our previous forward model [26] assumed zero RF phase across the entire FOV, which is a reasonable assumption for small FOVs and nonlossy samples. For the presented *in vivo* experiment, the assumption of a constant RF phase resulted in poor curve fit. The necessity of including dispersion was also evident from the asymmetry of the zero-gradient projection (not shown) collected at the start of each EPRI dataset. To accommodate the RF phase inhomogeneity, we modeled the spectral–spatial object as the voxel-by-voxel summation of two objects – one with absorption lineshape and the other with dispersion. The ratio of absorption and dispersion, at each voxel, was determined by the RF phase α as described in Eq. (A.1). To reduce the number of unknowns, all voxels at each site were assigned a single RF phase value, which is a reasonable assumption when spatial variations in the phase are gradual.

If $\mathscr{R}$ denotes the forward operator that converts a spectral–spatial object f to projection data Y then we can write

$$\mathscr{R}[f(\bar{\xi})] = Y(\bar{\xi}) \tag{1}$$

where vector $\bar{\xi}$ represents the unknowns – linewidth and RF phase at each site and spin density at each voxel of each site. In addition to spin density, linewidth, and RF phase, we assume the magnetic field sweep center h_c for each projection to be unknown. This assumption allows us to account for magnetic field drifts that may arise due to unforeseen factors such as animal motion or temperature fluctuations. Other variables arising from the nonideal behavior of the experimental setup, such as baseline drift, can also be included in the model as unknowns. Now the problem of multisite oximetry becomes a nonlinear minimization,

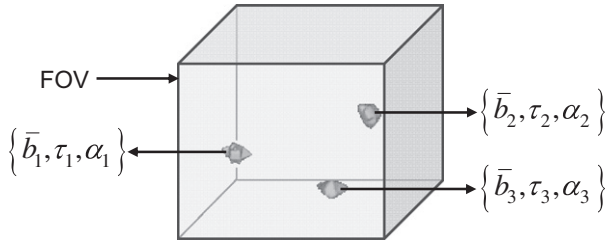

Fig. 1. Illustration of multisite oximetry for three probe sites. Each site covers only a small fraction of FOV. The unknowns at each site include spin densities $\bar{b}$ for all voxels, a linewidth τ, and an RF phase α.

$$\min_{\bar{\xi}, h_c} \frac{1}{2} \|\mathscr{R}[f(\bar{\xi})] - Y_n\|_2 \tag{2}$$

where Y_n represents noisy EPRI measurements.

Solving Eq. (2) for the entire spectral–spatial object can be numerically challenging. Moreover, for a small number of projections, the problem may become severely ill-conditioned. Therefore, it is important to reduce the size of $\bar{\xi}$ by identifying regions which carry spins. Here, we adopt a two stage approach where the first stage acts to reduce the number of unknowns. In our previous work, we used ℓ_1-regularized minimization of the approximate linear model to obtain a low-resolution distorted reconstruction, which provided approximate locations of the probe sites. Mathematically, it can be described as

$$\min_{\bar{b}} \frac{1}{2} \|\mathscr{R}[f(\bar{b})] - Y_n\|_2 + \lambda \|\bar{b}\|_1 \tag{3}$$

where $\bar{b}$ represents the unknown spin densities.

In Eq. (3), all unknowns other than spin density were assigned approximate user-defined values, resulting in a linear model for the data. But, the linearized approximation generates distorted spin density maps. The extent of distortion depends on the disagreement between the true values of the unknowns and their user-defined approximate values adopted in the linear model of Eq. (3). After reconstruction, these low-resolution spin density maps were segmented, and each segment was approximated by a sphere. All the spheres, collectively, were called region-of-interest (ROI). All voxels outside the ROI were assumed to carry no spins. This step, called stage 1, reduced the number of unknowns to a small fraction. In the next step, called stage 2, the unknown spin densities, linewidths, and RF phases were estimated using nonlinear least-squares minimization of Eq. (2) for the voxels belonging to the ROI. In the present work, we utilize 3D MRI to locate the particulate spin sites. Therefore, in stage 1, instead of relying on EPRI to find the ROI, we rely on MRI to define the ROI. The sub-millimeter resolution of MRI is capable of generating more accurate site locations.

The accuracy of pO_2 estimation depends on the total number of unknowns, the number of measurements, independence of measurements, and the SNR. From the previous literature [19,26], we conclude that projections at low gradient are less informative but possess higher SNR, and the projections at high gradient are more informative but possess lower SNR. In this work, we distributed the projections uniformly [36] between 0 and θ_{max}, with θ being the spectral angle. A convenient way to select θ_{max} is to choose as high a value as permitted by a preset limit on the SNR. Here, we adopted a value of θ_{max} such that the peak SNR (pSNR), defined by the ratio of peak-to-peak signal and the standard deviation of noise, at the highest gradient was greater than one. To estimate the number of projections for the *in vivo* application, we relied on a conservative estimate obtained from simulation studies.

2.2. Instrumentation

The details of coimaging instrumentation have been reported before [32]. Basic layout of the composite resonator used here is shown in Fig. 2a. The EPR resonator was based on a single-loop multi-gap design [37] with ID of 39 mm and length of 32 mm. The resonator efficiency, measured by using a perturbing metal sphere [38], was 17 $\mu T/\sqrt{W}$. The resonance frequency and quality factor of the unloaded resonator were measured to be 1.21 GHz and 200, respectively. Under the loaded conditions, however, the resonance frequency and the quality factor dropped to 1.15 GHz and 70, respectively. The NMR resonator was based on conventional solenoidal design with ID of 39 mm and length of 110 mm. A polyethylene tube, with ID of 34 mm, ran through both the res-

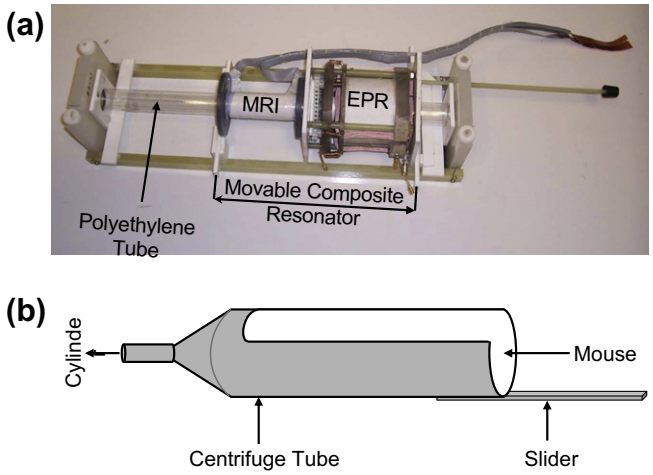

Fig. 2. A composite resonator and sample holder. EPR–NMR coimaging composite resonator assembly (a). Both resonators are connected end-to-end and slide together from one end to another, bringing the stationary sample inside one of the resonators. The polyethylene tubes acts as a housing for the sample holder. Sample holder made from 50 ml centrifuge tube (b). The nose cone end of the tube is connected to the gas cylinder while the other end is connected to a plastic strip, called slider, used to slide the centrifuge tube inside the polyethylene tube.

onators. The two resonators were attached together end-to-end so that they slid along the polyethylene tube as one unit. The entire assembly was securely placed at the designated location between the two main magnet poles of the EPR–NMR imager. The animal, resting in the sample holder (Fig. 2b), was slid into the polyethylene tube to a fixed location. Sliding the movable composite resonator assembly between extreme positions brought the animal in the center of either the EPR resonator or the NMR resonator.

The EPR measurements were conducted on a continuous wave imager operating at 1.15 GHz while the MRI measurements were performed at 16.18 MHz (380 mT). For the EPR measurements, no automatic coupling or automatic tuning was employed. A conventional automatic frequency control circuit was used to tune the RF source to the resonance frequency of the resonator. A fast scan, with scan rate of 20 Hz, was used to suppress breathing noise of the animal.

2.3. Animal model

A 25–30 g gray mouse was used for these studies. The mouse was implanted with lithium phthalocyanine (LiPc) [39], a widely used oxygen sensitive particulate EPR probe. The oxygen sensitivity calibration curve of LiPc indicated an anoxic linewidth of 11 μT and room air linewidth of 146 μT. The probe was implanted at three sites, one in each hind leg and one in the lower back. A total of 5–6 mg of probe was used, with each site having no more than 2 mg of probe. Before implantation, the mouse was anesthetized with ketamine (200 mg/kg b.w.) and xylazine (4 mg/kg b.w.) by intraperitoneal injection. The probe was implanted using a needle (16 gauge) and wire assembly. The ID of the needle was 1.2 mm while OD was 1.65 mm. The probe was weighed before being loaded into the tip of the needle. After loading, the needle was gently inserted 2–4 mm deep from the mouse skin to the position of interest. A metallic wire was slid into the other end of needle until its front end reached 1–2 mm from the tip of the needle where the material was loaded. Keeping the wire stationary, the needle was pulled completely out of the tissue, resulting in deposition of probe material. The wire was then pulled out. The procedure was repeated for all three sites.

To limit the motion of limbs during the measurements, two loops of paper tape were used to gently wrap the limbs against the torso. It is critical to suppress the animal motion because it can derail the entire coimaging process which relies on precise coregistration of EPRI and MRI. The mouse was placed in a sample holder made from a 50 ml centrifuge tube with ID 28 mm and length 117 mm. To facilitate direct access to the mouse, the top portion of the tube, along the longitudinal axis, was cut out as shown in Fig. 2b. The animal was placed with its snout facing the v-shaped end of the centrifuge tube which was connected to a gas cylinder via Teflon pipe. To guide the sample holder in and out of the polyethylene tube of the resonator assembly, the other open end of the tube was tied to an 18-in. long plastic strip, called slider. The sample holder carrying the mouse was slid into the polyethylene tube to a predefined fixed location of the composite resonator, and the nose cone end of the sample holder was connected to the tube supplying a mixture of either carbogen and isoflurane (0.5% by volume) or room air and isoflurane (0.5% by volume).

2.4. Data collection and processing

The EPRI data were collected first. The movable assembly of the composite resonator was moved to one extreme so that the FOV was within the sensitive region of the EPR resonator. The parameters used to collect EPR data were: RF power = 100 mW; FOV = $65 \times 65 \times 65$ mm^3; spectral window $\Delta H = 0.25$ mT; field modulation amplitude = 10 μT; $\theta_{max} = 81°$; maximum gradient strength = 24.3 μT/mm; reconstruction matrix size = $32 \times 32 \times 32$; and number of projections per dataset = 60. A total averaging time (in seconds) for each projection was proportional to $\lceil|\tan\theta| + 0.5\rceil$, with $\lceil.\rceil$ denoting the next higher integer. This variable sweep time allowed to partially suppress the degradation of SNR for high gradient projections. The parameters for MRI data collection were: receiver bandwidth = 10 kHz; TE = 13 ms; TR = 100 ms; pulse sequence = 3D gradient-echo; FOV = $65 \times 65 \times 65$ mm^3; 3D matrix size = $128 \times 128 \times 128$; slice thickness = 0.5 mm; number of excitations = 1; total acquisition time = 28 min.

The data were processed in Matlab (Mathworks, MA) on a 2.27 GHz Intel Core™ i5 processor coupled with 4 GB of memory. Approximate processing time for a 60-projection dataset was 12 min. The site locations, read from MRI, along with the EPRI projection data were fed to a Matlab code. First, all the voxels residing within the 6 mm-radius spheres centered around the site locations indicated by MRI were marked as ROI. Later, the *lsqnonlin* function was used to solve for unknowns, which in our case included spin densities for all voxels at each site, linewidth at each site, RF phase at each site, and center field drift for each projection. Total number of unknowns was only 435. Each collected projection had 1024 samples, but was decimated to 256 samples for faster computations. The decimation issue, although not handled in this work, can be overcome by tweaking hardware settings so that only 256 points are collected in each scan, or by expanding computational resources (for example, by using multiple nodes for parallel computation) so that projections with 1024 points can be processed in reasonable time. This improvement, when implemented, would result in further reduction in data collection times for multisite EPR oximetry.

3. Results

3.1. Simulation

The purpose of this simulation study is to demonstrate the impact of ROI size on the estimation of linewidth τ. The results show that the selection of a smaller ROI leads to more accurate estimation of τ. This impact motivates selecting a more compact ROI

using the high-resolution MRI reconstruction as opposed to the low-resolution EPRI reconstruction.

A digital phantom consisting of eight sites was used. The location of each site was chosen randomly on a $32 \times 32 \times 32$ grid for each of 10 trial runs. There was no constraint on the distribution of site locations except that no two sites were allowed to touch or overlap. Therefore, we enforced a minimum distance of one voxel (2 mm) between the neighboring sites. The peak-to-peak linewidths for the eight sites were selected to be 12 μT, 16 μT, 20 μT, 24 μT, 28 μT, 32 μT, 36 μT, and 40 μT. The size of each site was $2 \times 2 \times 2$ voxels. The spin density (0.5–1.0) and the RF phase $(0 - \pi/2)$ values across each site were constants and were chosen randomly for each trial. Other simulation parameters, including FOV size, gradient strength, and number of projections, were identical to the ones used for the *in vivo* experiment. The value of pSNR for the zero-gradient projection was selected to be 12.

Fig. 3 shows a typical simulated input phantom comprising eight sites and the corresponding reconstructed linewidth map. Fig. 4 shows the curve fitting results for a projection corresponding to the gradient of 24.3 μT/mm. The simulation results, demonstrating the impact of ROI size on the estimation of τ, are summarized in Fig. 5. The results from an ROI comprised of 2.5 mm-radius spheres are compared with the results from an ROI comprising of 5.0 mm-radius spheres, both selected around the true locations.

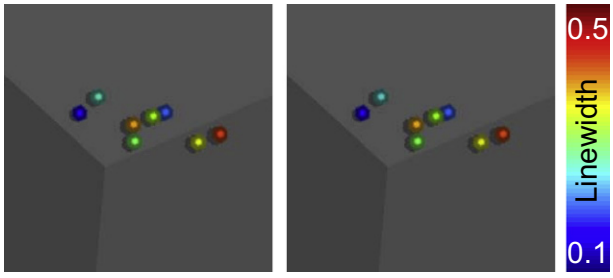

Fig. 3. Input (left) and reconstructed (right) 3D linewidth maps for one of the realizations of the eight-site digital phantom. An ROI consisting of eight 2.5 mm-radius spheres was used. The minimum distance between the sites was one voxel (2 mm). The color at each site encodes the linewidth value. (For interpretation of the references to color in this figure legend, the reader is referred to the web version of this article.)

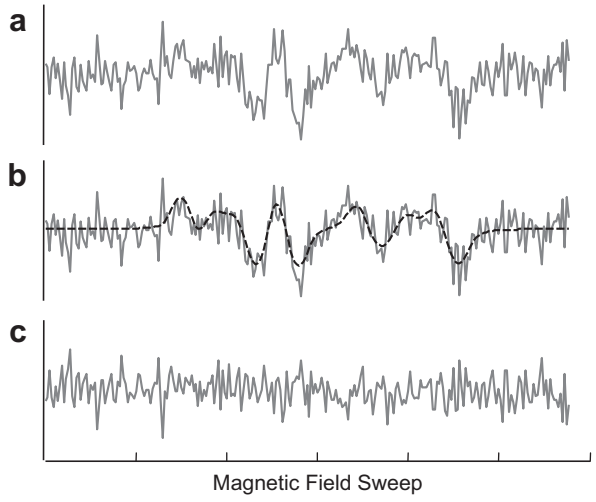

Fig. 4. Curve fit for one of the projections for the digital phantom shown in Fig. 3. A projection simulated at 24.3 μT/mm gradient strength (a); dotted line indicates the nonlinear least-squares fit using the proposed forward model (b); and the residual (c).

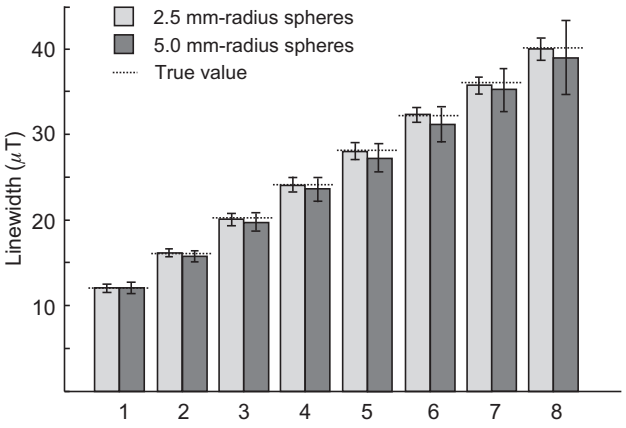

Fig. 5. Simulation results illustrating the impact of ROI size on the estimation of linewidth τ at each of the eight sites. In one case, the ROI consisted of 2.5 mm-radius spheres, while in the other case the ROI consisted of 5.0 mm-radius spheres. In both the cases, the spheres were centered around the true locations. A total of 10 trials were considered.

3.2. In vivo oximetry

A total of three datasets were collected under carbogen breathing. Total acquisition time for each dataset was approximately 12 min. After collecting the data under carbogen breathing, the breathing mixture was switched to room air, and three more datasets were collected after a delay of 5 min. Under room air breathing, all parameters were kept the same except the sweep time. There was visible sharpening of EPR spectrum under room air breathing, which resulted in improved SNR. Therefore, the sweep time was reduced to half without any visible degradation of SNR. The acquisition for each dataset, under room air breathing, took approximately 6 min. For the EPRI data, the pSNR for the zero-gradient projection was 12 and 21 under carbogen and room air breathing environments, respectively.

After the EPRI measurements, the movable assembly of the composite resonator was slid to the other extreme such that the FOV was within the sensitive region of the NMR resonator. The main magnetic field was switched to 380 mT. The field was allowed to stabilize for 10 min before collecting MRI data. Fig. 6 shows three axial MRI slices each passing through one of the spin sites. Approximate spin density maps, computed from Eq. (3), for one of the datasets collected under room air conditions, are also shown along with the corresponding fused images.

First, the sites were recognized from the MRI reconstruction. In this case, we used a 6 mm-radius sphere to represent each site. All the voxels inscribed within these spheres were collectively called ROI. The size and location of each sphere were defined by the user and were based on the MRI information. Later, the nonlinear least-squares optimization (Eq. (2)) was solved for the entire ROI to estimate the unknown linewidths, spin densities, RF phases, and magnetic field drifts. Fig. 7 shows, from left to right, the isosurface rendering of 3D MRI, 3D EPRI spin density map generated from stage 2, and the overlay of the two. Fig. 8 displays three axial slices of MRI superimposed with estimated spin density and linewidth maps generated by stage 2 of multisite oximetry. Both Figs. 7 and 8 belong to a dataset with room air breathing condition. Fig. 9 shows the curve fit results for one of the projections collected at 24.3 μT/mm.

For comparison, the low-resolution distorted EPR images were also used to define the ROI. To accommodate for the blur and offset of the EPR images from stage 1 (Fig. 6b), a larger ROI, comprised of 9 mm-radius spheres, was selected. Any attempt to select an ROI with smaller radii resulted in visible structure in the curve fit residual, indicating the presence of spins outside the designated ROI.

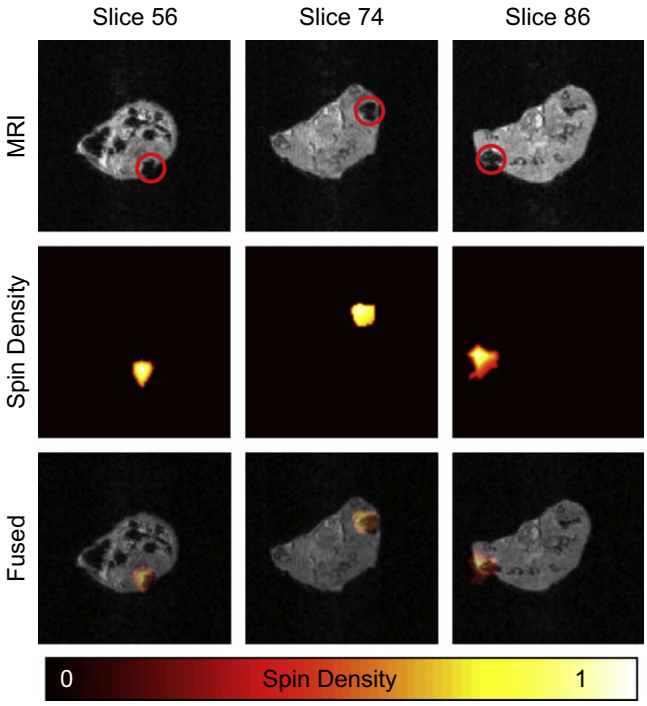

Fig. 6. MRI overlaid with low-resolution distorted EPRI spin density map. The first row shows three axial MRI slices with each passing through one of the spin deposit sites. Slices 56, 74, and 86 display back, right leg, and left leg implants, respectively. The red circles highlight the implant locations. The second row displays the respective slices from the distorted low-resolution EPRI spin density map from stage 1. Third row shows the superposition of the top two rows. The areas with no signal from both EPRI and MRI images were partially cropped resulting in a 48×48 mm^2 display. (For interpretation of the references to color in this figure legend, the reader is referred to the web version of this article.)

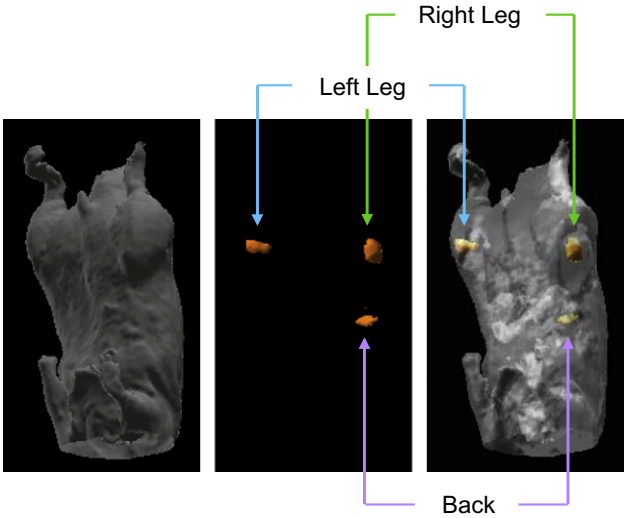

Fig. 7. Isosurface rendering of MRI and EPRI spin density map. From left to right, 3D MRI, final 3D EPRI spin density map generated from Eq. (2), and superposition of the two. For the EPRI reconstruction, the ROI was selected from the MRI.

The results for pO_2 estimation are summarized in Fig. 10 for both the ROIs based on the MRI and low-resolution EPR reconstruction.

4. Discussion

We have demonstrated the applicability of multisite EPR oximetry in an EPR–NMR coimaging framework. The multisite EPR

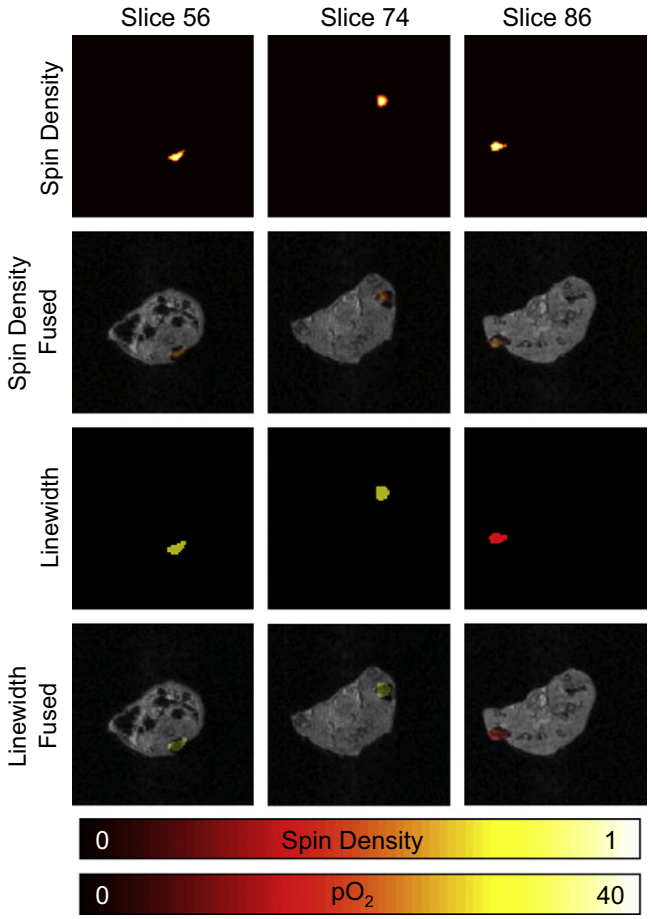

Fig. 8. MRI and multisite oximetry results superimposed. The first row shows three slices from the stage 2 EPRI spin density map. The third row shows the same three slices from the stage 2 EPRI pO_2 map. The second and fourth rows display fused EPRI–MRI for spin density and pO_2, respectively. The areas with no signal from both EPRI and MRI images were partially cropped resulting in 48×48 mm^2 display.

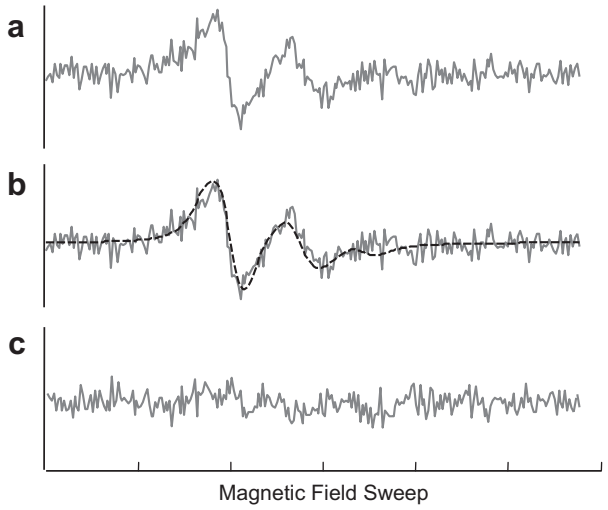

Fig. 9. Curve fit for one of the projections collected under room air breathing. A projection measured at 24.3 μT/mm gradient strength (a); dotted line indicates the nonlinear least-squares fit using the proposed forward model (b); and the residual (c).

oximetry allows for the *in vivo* oxygenation monitoring of multiple regions simultaneously while MRI provides the anatomic details of the body. The existing coimaging setup allows the inherent coreg-

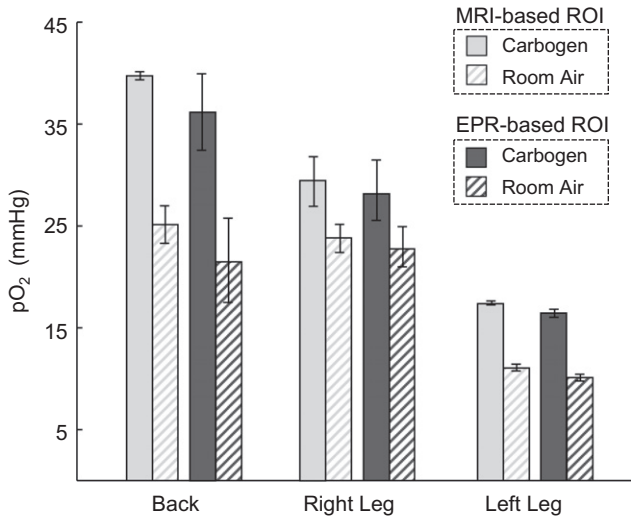

Fig. 10. Results from *in vivo* multisite oximetry. The pO_2 values under carbogen breathing are compared with the pO_2 under room air breathing. Also, the results from two different ROIs, one selected from the MRI (6 mm-radius spheres) and the other selected from low-resolution EPR (9 mm-radius spheres), are compared.

istration of two imaging modalities. In addition to anatomic details, MRI reconstruction also provides precise locations of probe implants, facilitating the data processing for the multisite oximetry.

The simulation studies presented in this work illustrate the impact of ROI size on the estimation of unknown parameters. A rather modest expansion of ROI can have dramatic effect on the number of unknowns. For the simulation study, increasing the radius of each of the eight ROI spheres from 2.5 mm to 5.0 mm increased the total number of unknowns from 140 to 524. This increase make the inverse problem of estimating unknown parameters more ill-conditioned for a given number of measurements. Therefore, it is advantageous to reduce the number of unknowns. EPR images from stage 1 prompt a selection with larger ROI to accommodate for the uncertainties, due to low-resolution and distortion, in site locations. The MRI reconstruction, with it higher resolution, has the potential to select more compact ROI and hence positively influence the estimation process. Also, selecting the ROI from the low-resolution EPRI may become troublesome when the distance between the neighboring sites is small. Fig. 5 summarizes the impact of ROI size on the estimation of τ. By doubling the radius of spheres that define the ROI, the standard deviation of estimated τ is more than doubled, for at least some of the sites.

Fig. 6 shows three MRI slices and the corresponding low-resolution EPRI slices reconstructed from the linearized approximation of the forward model. The low-resolution EPRI was reconstructed on a $16 \times 16 \times 16$ grid but was later linearly interpolated to a $128 \times 128 \times 128$ grid to match the MRI grid. This stage, called stage 1, generates a low-resolution reconstruction with the sole purpose of detecting the approximate site locations. This was the approach we previously adopted [26] in the absence of MRI, and has been used here to draw a comparison with the MRI-based selected of the ROI. In the presence of MRI, however, it is logical to unitize the high-resolution MRI reconstruction in stage 1 to select site locations, as depicted in Fig. 6. The low-resolution stage 1 EPRI spin density maps were, nevertheless, used to narrow the size of the MRI search volume. Visually searching for the probe site locations in MRI alone can be difficult because both particulate probe implants and several anatomic structures of the body manifest themselves in MRI as regions with no signal, and thus can be mistaken for each other. The stage 1 EPRI facilitated the search process by providing approximate site locations, and MRI further refined the implant localization by searching in the proximity of the locations provided by stage 1 EPRI.

In the second stage, called stage 2, spin densities and linewidths were estimated by solving Eq. (2) using nonlinear least-squares minimization. Figs. 7 and 8 show the reconstruction results for the dataset used for Fig. 6. Fig. 7 displays the 3D images, individual and superimposed, for MRI and stage 2 EPRI spin density map. For surface rendering of EPRI and MRI, thresholds of 25% and 15% of the peak values were applied, respectively. Fig. 8 shows slices #56 (back), #74 (right leg), and #86 (left leg) for both spin density and linewidth maps. As evident from this figure, the MRI and EPRI reconstructions are automatically coregistered without additional processing.

Fig. 9 shows curve fit results for one the 60 projections. Fig. 10 summarizes the oximetry results for both MRI- and EPR-based selections of the ROI. Again, the ROI selection based on MRI generates lower variances in the estimated τ. The pO_2 variation across two different breathing conditions is in line with the previous studies [40] which have shown an increase in tissue oxygenation under carbogen breathing. The reason for pO_2 variation across different sites can be, at least partially, attributed to the depth of the implants in the body. For instance, the implant in the left leg, which displays the lowest pO_2 value, is located more subcutaneously as compared to the implant in the right leg which is located intramuscularly, as revealed by MRI reconstruction. Previously [41], it has been reported that intramuscular pO_2 tends to be higher than subcutaneous pO_2 for an extended duration after the invasive probe implantation procedure. In addition to the location, the variability in the condition of a fresh wound, occurred due to needle insertion, may also have contributed to the pO_2 variation across different sites. This basic experiment merely provides a proof of concept. Further studies, in the context of specific applications, are required to further analyze the pO_2 values at each specific site under specific conditions.

Since the acquisition time for multisite oximetry is of the order of minutes as opposed to hours required for spectral–spatial imaging, it provides opportunities for many interesting *in vivo* applications. For example, this methodology can be used to study the response of tumor oxygenation to a gradual change in the breathing environment. Also, using multiple implants, it would be possible to compare tumor oxygenation with the healthy tissue.

5. Conclusions

We have implemented EPR multisite oximetry for *in vivo* monitoring of pO_2 values simultaneously across multiple regions. Our approach improves the previously proposed EPR multisite methods by generalizing the data model to take into account the RF phase variations inside the resonator. In addition, coregistered MRI is utilized to accurately determine the locations of spin sites. Spherical regions selected around these locations are then used in the model to extract the linewidth and the spin densities. As compared to conventional spectral–spatial imaging, the data collection time is reduced by an order of magnitude. This preliminary *in vivo* experiment illustrates potential as well as applicability of the method to meaningful physiological applications where time constraint is critical.

Acknowledgments

We thank Eric Kesselring for technical assistance and Craig Hemann for preparation of LiPc. This work was supported by NIH Grants EB0890, EB4900, and EB008836.

Appendix A

Here, we describe EPRI data model which relates the unknowns, belonging to either a spectral–spatial object or the EPR measurement process, to the collected CW projection data. We make following assumptions about the object and the measurement process: (i) the 3D object is discretized into K voxels in spatial domain; (ii) lineshape at each voxel is a Lorentzian with both absorption and dispersion components; (iii) ratio of absorption and dispersion components at each voxel depends on the unknown RF phase at that voxel; (iv) modulation amplitude is small and the detection process generates the first derivative of lineshape without distortion; (v) there is no signal distortion due to RF power saturation; and (vi) the main magnetic field is swept in discrete steps for each projection.

The kth voxel of spectral–spatial object f can be written as

$$\begin{aligned} f_k &= f_{a,k} + f_{d,k}, \quad \text{for } 1 \leqslant k \leqslant K \\ &= \frac{b_k \tau_k \cos\alpha_k}{(h+h_c)^2+\tau_k^2} + \frac{-b_k(h+h_c)\sin\alpha_k}{(h+h_c)^2+\tau_k^2} \end{aligned} \tag{A.1}$$

where subscripts a and d represent absorption and dispersion respectively; τ_k, b_k, and α_k denote linewidth, spin density, and RF phase at the kth voxel, respectively; h denotes magnetic field sweep centered around resonance field; and h_c represents the shift in the center of magnetic field sweep.

Let $(\rho, \eta, \phi, \theta)$ represent the polar coordinate system defined below,

$$\begin{aligned} x &= \frac{\rho}{\gamma}\cos\eta\sin\phi\sin\theta \\ y &= \frac{\rho}{\gamma}\sin\eta\sin\phi\sin\theta \\ z &= \frac{\rho}{\gamma}\cos\phi\sin\theta \\ h &= \rho\cos\theta \end{aligned} \tag{A.2}$$

where $\gamma = -\Delta H/\Delta L$ with ΔH being the spectral window and ΔL being the spatial FOV.

The 4D Radon transform (RT) of the object f can be obtained by integrating the object along a hyper-plane defined by

$$\rho = \gamma((x\cos\eta + y\sin\eta)\sin\phi + z\cos\phi)\sin\theta + h\cos\theta \tag{A.3}$$

which can be written in terms of magnetic field gradients

$$\rho = -(g_x x + g_y y + g_z z)\cos\theta + h\cos\theta \tag{A.4}$$

where g_x, g_y, and g_z represents x, y, and z components of magnetic field gradient defined below

$$\begin{aligned} g_x &= -\gamma\tan\theta\ (\cos\eta\sin\phi) \\ g_y &= -\gamma\tan\theta\ (\sin\eta\sin\phi) \\ g_z &= -\gamma\tan\theta\ (\cos\phi) \end{aligned} \tag{A.5}$$

By $m_k \equiv (g_x x + g_y y + g_z z)$ and $\rho_k \equiv -m_k\cos\theta + h\cos\theta$, we can write the RT as

$$\begin{aligned} p &= c_0 \sum_{k=1}^{K} \int_h \int_{z_k} \int_{y_k} \int_{x_k} f_k \delta(\rho_k + m_k\cos\theta - h\cos\theta)\,dx_k\,dy_k\,dz_k\,dh \\ &= c_0 \sum_{k=1}^{K} \frac{1}{|\cos\theta|} \int_h \int_{z_k} \int_{y_k} \int_{x_k} f_k \delta(h - m_k - \rho_k/\cos\theta)\,dx_k\,dy_k\,dz_k\,dh \end{aligned} \tag{A.6}$$

where c_0, a positive real number, is an arbitrary scaling factor. Using Eqs. (A.1) and (A.6), the RT for absorption component becomes

$$\begin{aligned} p_a &= \sum_{k=1}^{K} \frac{c_0}{|\cos\theta|} \int_h \int_{z_k} \int_{y_k} \int_{x_k} \frac{b_k\tau_k\cos\alpha_k}{(h+h_c)^2+\tau_k^2} \delta(h - m_k - \rho_k/\cos\theta) \\ &\quad \times dx_k\,dy_k\,dz_k\,dh \\ &= \sum_{k=1}^{K} \frac{c_0}{|\cos\theta|} \int_{z_k} \int_{y_k} \int_{x_k} \frac{b_k\tau_k\cos\alpha_k}{(m_k+\rho_k/\cos\theta+h_c)^2+\tau_k^2}\,dx_k\,dy_k\,dz_k \end{aligned} \tag{A.7}$$

For small modulation amplitudes, the collected projection data can be approximated by the first derivative of RT computed in (A.7) scaled by $\cos^2\theta$. Therefore,

$$\begin{aligned} \hat{p}_a &= \cos^2\theta \frac{d}{d\rho_k} p_a \\ &= \sum_{k=1}^{K} \frac{c_0\cos^2\theta}{|\cos\theta|} \frac{d}{d\rho_k} \int_{z_k} \int_{y_k} \int_{x_k} \\ &\quad \times \frac{b_k\tau_k\cos\alpha_k}{(m_k+\rho_k/\cos\theta+h_c)^2+\tau_k^2}\,dx_k\,dy_k\,dz_k \end{aligned} \tag{A.8}$$

which using Leibniz's rule becomes

$$\begin{aligned} \hat{p}_a &= \sum_{k=1}^{K} \frac{c_0\cos^2\theta}{|\cos\theta|} \int_{z_k} \int_{y_k} \int_{x_k} \\ &\quad \times \frac{\partial}{\partial\rho_k} \left(\frac{b_k\tau_k\cos\alpha_k}{(m_k+\rho_k/\cos\theta+h_c)^2+\tau_k^2} \right) dx_k\,dy_k\,dz_k \end{aligned} \tag{A.9}$$

After taking the derivative and three integrals, Eq. (A.9) yields

$$\hat{p}_a = \sum_{k=1}^{K} c_k b_k \tau_k (a_{1,k} + a_{2,k})\cos\alpha_k \tag{A.10}$$

where

$$\begin{aligned} c_k &= \frac{c_0\cos\theta}{g_x g_y g_z |\cos\theta|} \\ a_{1,k} &= v_{1,k}\tan^{-1}(v_{1,k}) + v_{2,k}\tan^{-1}(v_{2,k}) + v_{3,k}\tan^{-1}(v_{3,k}) \\ &\quad + v_{4,k}\tan^{-1}(v_{4,k}) - v_{5,k}\tan^{-1}(v_{5,k}) - v_{6,k}\tan^{-1}(v_{6,k}) \\ &\quad - v_{7,k}\tan^{-1}(v_{7,k}) - v_{8,k}\tan^{-1}(v_{8,k}) \\ a_{2,k} &= -(1/2)\left[\log\left(1+v_{1,k}^2\right) + \log\left(1+v_{2,k}^2\right) + \log\left(1+v_{3,k}^2\right)\right. \\ &\quad + \log\left(1+v_{4,k}^2\right) - \log\left(1+v_{5,k}^2\right) - \log\left(1+v_{6,k}^2\right) \\ &\quad \left. - \log\left(1+v_{7,k}^2\right) - \log\left(1+v_{8,k}^2\right)\right] \end{aligned} \tag{A.11}$$

with

$$\begin{aligned} v_{1,k} &= \frac{1}{\tau_k}(g_x\lfloor x_k\rfloor + g_y\lfloor y_k\rfloor + g_z\lceil z_k\rceil + \rho_k/\cos\theta + h_c) \\ v_{2,k} &= \frac{1}{\tau_k}(g_x\lfloor x_k\rfloor + g_y\lceil y_k\rceil + g_z\lfloor z_k\rfloor + \rho_k/\cos\theta + h_c) \\ v_{3,k} &= \frac{1}{\tau_k}(g_x\lceil x_k\rceil + g_y\lfloor y_k\rfloor + g_z\lfloor z_k\rfloor + \rho_k/\cos\theta + h_c) \\ v_{4,k} &= \frac{1}{\tau_k}(g_x\lceil x_k\rceil + g_y\lceil y_k\rceil + g_z\lceil z_k\rceil + \rho_k/\cos\theta + h_c) \\ v_{5,k} &= \frac{1}{\tau_k}(g_x\lfloor x_k\rfloor + g_y\lfloor y_k\rfloor + g_z\lfloor z_k\rfloor + \rho_k/\cos\theta + h_c) \\ v_{6,k} &= \frac{1}{\tau_k}(g_x\lfloor x_k\rfloor + g_y\lceil y_k\rceil + g_z\lceil z_k\rceil + \rho_k/\cos\theta + h_c) \\ v_{7,k} &= \frac{1}{\tau_k}(g_x\lceil x_k\rceil + g_y\lfloor y_k\rfloor + g_z\lceil z_k\rceil + \rho_k/\cos\theta + h_c) \\ v_{8,k} &= \frac{1}{\tau_k}(g_x\lceil x_k\rceil + g_y\lceil y_k\rceil + g_z\lfloor z_k\rfloor + \rho_k/\cos\theta + h_c). \end{aligned} \tag{A.12}$$

For the dispersion component, an expression equivalent of Eq. (A.9) can be written as

$$\hat{p}_d = \sum_{k=1}^{K} \frac{c_0 \cos^2\theta}{|\cos\theta|} \int_{z_k}\int_{y_k}\int_{x_k} \times \frac{\partial}{\partial \rho_k}\left(\frac{-b_k(m_k+\rho_k/\cos\theta+h_c)\sin\alpha_k}{(m_k+\rho_k/\cos\theta+h_c)^2+\tau_k^2}\right) dx_k\, dy_k\, dz_k \quad (A.13)$$

which after taking the derivative and three integrals yields

$$\hat{p}_d = \sum_{k=1}^{K} c_k b_k \tau_k (d_{1,k}+d_{2,k}+d_{3,k})\sin\alpha_k \quad (A.14)$$

where

$$\begin{aligned} d_{1,k} &= -\big[\tan^{-1}(v_{1,k})+\tan^{-1}(v_{2,k})+\tan^{-1}(v_{3,k}) \\ &\quad +\tan^{-1}(v_{4,k})-\tan^{-1}(v_{5,k})-\tan^{-1}(v_{6,k}) \\ &\quad -\tan^{-1}(v_{7,k})-\tan^{-1}(v_{8,k})\big] \\ d_{2,k} &= -(1/2)\Big[v_{1,k}\log\left(1+v_{1,k}^2\right)+v_{2,k}\log\left(1+v_{2,k}^2\right)+v_{3,k}\log\left(1+v_{3,k}^2\right) \\ &\quad +v_{4,k}\log\left(1+v_{4,k}^2\right)-v_{5,k}\log\left(1+v_{5,k}^2\right)-v_{6,k}\log\left(1+v_{6,k}^2\right) \\ &\quad -v_{7,k}\log\left(1+v_{7,k}^2\right)-v_{8,k}\log\left(1+v_{8,k}^2\right)\Big] \\ d_{3,k} &= v_{1,k}+v_{2,k}+v_{3,k}+v_{4,k}-v_{5,k}-v_{6,k}-v_{7,k}-v_{8,k} \end{aligned} \quad (A.15)$$

Therefore, for an inhomogeneous RF phase, EPR projection data $Y(\eta, \phi, \theta, \rho)$ can represented as

$$\begin{aligned} Y(\eta,\phi,\theta,\rho) &= \hat{p}_a + \hat{p}_d \\ Y_n(\eta,\phi,\theta,\rho) &= Y(\eta,\phi,\theta,\rho) + n(\eta,\phi,\theta,\rho) \end{aligned} \quad (A.16)$$

where n is additive white Gaussian noise with variance σ^2.

References

[1] J. Raymond, D. Segre, The effect of oxygen on biochemical networks and the evolution of complex life, Science 311 (2006) 1764–1767.
[2] R. Berner, J. VandenBrooks, P. Ward, Oxygen and evolution, Science 316 (2007) 557–558.
[3] R. Springett, H. Swartz, Measurement of oxygen in vivo: overview and perspectives on methods to measure oxygen within cells and tissues, Antioxid. Redox Signaling 9 (2007) 1295–1301.
[4] D. Vikram, J. Zweier, P. Kuppusamy, Methods for noninvasive imaging of tissue hypoxia, Antioxid. Redox Signaling 9 (2007) 1745–1756.
[5] R. Ahmad, P. Kuppusamy, Theory, instrumentation, and applications of electron paramagnetic resonance oximetry, Chem. Rev. 110 (2010) 3212–3236.
[6] W. Subczynski, J. Hyde, The diffusion-concentration product of oxygen in lipid bilayers using the spin-label T1 method, Biochim. Biophys. Acta 643 (1981) 283–291.
[7] H. Swartz, S. Boyer, P. Gast, J. Glockner, H. Hu, K. Liu, M. Moussavi, S. Norby, N. Vahidi, T. Walczak, M. Wu, R. Clarkson, Measurements of pertinent concentrations of oxygen in vivo, Magn. Reson. Med. 20 (1991) 333–339.
[8] J. Zweier, P. Kuppusamy, Electron paramagnetic resonance measurements of free radicals in the intact beating heart: a technique for detection and characterization of free radicals in whole biological tissues, Proc. Natl. Acad. Sci. USA 85 (1988) 5703–5707.
[9] H. Halpern, C. Yu, M. Peric, E. Barth, G. Karczmar, J. River, D. Grdina, B. Teicher, Measurement of differences in pO2 in response to perfluorocarbon/carbogen in FSa and NFSa murine fibrosarcomas with low-frequency electron paramagnetic resonance oximetry, Radiat. Res. 145 (1996) 610–618.
[10] R. Pandian, N. Parinandi, G. Ilangovan, J. Zweier, P. Kuppusamy, Novel particulate spin probe for targeted determination of oxygen in cells and tissues, Free Radical Biol. Med. 35 (2003) 1138–1148.
[11] W. Subczynski, H. Swartz, Biomedical EPR, Part A: Free Radicals, Metals, Medicine, and Physiology, Kluwer Academic, 2005.
[12] F. Goda, G. Bacic, J. Hara, B. Gallez, H. Swartz, J. Dunn, The relationship between partial pressure of oxygen and perfusion in two murine tumors after X-ray irradiation: a combined gadopentetate dimeglumine dynamic magnetic resonance imaging and in vivo electron paramagnetic resonance oximetry study, Cancer Res. 56 (1996) 3344–3349.
[13] G. Ilangovan, T. Liebgott, V. Kutala, S. Petryakov, J. Zweier, P. Kuppusamy, EPR oximetry in the beating heart: myocardial oxygen consumption rate as an index of postischemic recovery, Magn. Reson. Med. 51 (2004) 835–842.
[14] X. Zhao, G. He, Y. Chen, R. Pandian, P. Kuppusamy, J. Zweier, Endothelium-derived nitric oxide regulates postischemic myocardial oxygenation and oxygen consumption by modulation of mitochondrial electron transport, Circulation 111 (2005) 2966–2972.
[15] M. Maltempo, Differentiation of spectral and spatial components in EPR imaging using 2-D image reconstruction algorithms, J. Magn. Reson. 69 (1986) 156–161.
[16] H. Sato-Akaba, Y. Kuwahara, H. Fujii, H. Hirata, Half-life mapping of nitroxyl radicals with three-dimensional electron paramagnetic resonance imaging at an interval of 3.6 seconds, Anal. Chem. 81 (2009) 75017506.
[17] Y. Deng, S. Petryakov, G. He, E. Kesselring, P. Kuppusamy, J.L. Zweier, Fast 3D spatial EPR imaging using spiral magnetic field gradient, J. Magn. Reson. 185 (2007) 283–290.
[18] J. Joshi, J. Ballard, G. Rinard, R. Quine, S. Eaton, G. Eaton, Rapid-scan EPR with triangular scans and fourier deconvolution to recover the slow-scan spectrum, J. Magn. Reson. 175 (2005) 44–51.
[19] S. Som, L. Potter, R. Ahmad, P. Kuppusamy, A parametric approach to spectralspatial EPR imaging, J. Magn. Reson. 186 (2007) 1–10.
[20] Y. Deng, R. Pandian, R. Ahmad, P. Kuppusamy, J. Zweier, Application of magnetic field over-modulation for improved EPR linewidth measurements using probes with Lorentzian lineshape, J. Magn. Reson. 181 (2006) 254–261.
[21] J. Hyde, H. Mchaourab, T. Camenisch, J. Ratke, R. Cox, W. Froncisz, EPR detection by time-locked sub-sampling, Rev. Sci. Instrum. 69 (1998) 2622–2628.
[22] S. Subramanian, K. Matsumoto, J. Mitchell, M. Krishna, Radio frequency continuous-wave and time-domain EPR imaging and overhauser-enhanced magnetic resonance imaging of small animals: instrumental developments and comparison of relative merits for functional imaging, NMR Biomed. 17 (2004) 263–294.
[23] A. Smirnov, S. Norby, R. Clarkson, H. Swartz, Simultaneous multi-site EPR spectroscopy in vivo, Magn. Reson. Med. (1993) 213–220.
[24] O. Grinberg, A. Smirnov, H. Swartz, High spatial resolution multi-site EPR oximetry: the use of a convolution-based fitting method, J. Magn. Reson. 152 (2001) 247–258.
[25] B. Williams, H. Hou, O. Grinberg, E. Demidenko, H. Swartz, High spatial resolution multisite EPR oximetry of transient focal cerebral ischemia in the rat, Antioxid. Redox Signaling (2007) 1691–1698.
[26] S. Som, L. Potter, R. Ahmad, D. Vikram, P. Kuppusamy, EPR oximetry in three spatial dimensions using sparse spin distribution, J. Magn. Reson. 193 (2008) 210–217.
[27] K. Matsumoto, F. Hyodo, F. Matsumoto, A. Koretsky, A. Sowers, J. Mitchell, M. Krishna, High-resolution mapping of tumor redox status by magnetic resonance imaging using nitroxides as redox-sensitive contrast agents, Clin. Cancer Res. 12 (2006) 2455–2462.
[28] D. Lurie, G. Davies, M. Foster, J. Hutchison, Field-cycled pedri imaging of free radicals with detection at 450 mt, Magn. Reson. Imag. 23 (2005) 175–181.
[29] G. He, Y. Deng, H. Li, P. Kuppusamy, J. Zweier, EPR/MRI co-imaging for anatomic registration of free-radical images, Magn. Reson. Med. 47 (2002) 571–578.
[30] S. Matsumoto, M. Nagai, K. Yamada, F. Hyodo, K. Yasukawa, M. Muraoka, H. Hirata, M. Ono, H. Utsumi, A composite resonator assembly suitable for EPR/MRI coregistration imaging, Concepts Magn. Reson. 25 (2005) 1–11.
[31] Y. Kawada, H. Hirata, H. Fujii, Use of multi-coil parallel-gap resonators for co-registration EPR/NMR imaging, J. Magn. Reson. 184 (2007) 29–38.
[32] G. Caia, A. Samouilov, E. Kesselring, S. Petryakov, T. Wasowicz, J. Zweier, Development of a hybrid EPR/NMR coimaging system, Magn. Reson. Med. 58 (2007) 156–166.
[33] M. Elas, R. Bell, D. Hleihel, E. Barth, C. McFaul, C.H.J. Bielanska, K. Pustelny, K. Ahn, C. Pelizzari, M. Kocherginsky, H. Halpern, Electron paramagnetic resonance oxygen image hypoxic fraction plus radiation dose strongly correlates with tumor cure in FSa fibrosarcomas, Int. J. Radiat. Oncol., Biol., Phys. 71 (2008) 542–549.
[34] S. Matsumoto, F. Hyodo, S. Subramanian, N. Devasahayam, J. Munasinghe, E. Hyodo, C. Gadisetti, J.A. Cook, J.B. Mitchell, M.C. Krishna, Low-field paramagnetic resonance imaging of tumor oxygenation and glycolytic activity in mice, J. Clin. Invest. 118 (2008) 1965–1973.
[35] A. Smirnov, T. Smirnova, Convolution-based Algorithms: From Analysis to Rotational Dynamics to EPR Oximetry and Protein Distance Measurements, Kluwer Academic, 2004. pp. 277–348 (Chapter 6).
[36] R. Ahmad, D. Vikram, B. Clymer, L. Potter, Y. Deng, P. Srinivasan, J. Zweier, P. Kuppusamy, Uniform distribution of projection data for improved reconstruction quality of 4D EPR imaging, J. Magn. Reson. 187 (2007) 277–287.
[37] S. Petryakov, A. Samouilov, E. Kesselring, T. Wasowicz, G. Caia, J. Zweier, Single loop multi-gap resonator for whole body EPR imaging of mice at 1.2 GHz, J. Magn. Reson. 188 (2007) 68–73.
[38] J. Freed, D. Leniart, J. Hyde, Theory of saturation and double resonance effects in ESR spectra. III. Rf coherence and line shapes, J. Chem. Phys. 47 (1967) 2762–2773.
[39] P. Turek, J. Andre, A. Giraudeau, J. Simon, Preparation and study of a lithium phthalocyanine radical – optical and magnetic-properties, Chem. Phys. Lett. 137 (1987) 471–476.
[40] W. Stein, S. Subramanian, J. Mitchell, M. Krishna, EPR imaging of vascular changes in oxygen in response to carbogen breathing, Adv. Exp. Med. Biol. 510 (2003) 231–236.
[41] N. Khan, H. Hou, P. Hein, R. Comi, J. Buckey, O. Grinberg, I. Salikhov, S. Lu, H. Wallach, H. Swartz, Black magic and EPR oximetry: from lab to initial clinical trials, Adv. Exp. Med. Biol. 566 (2005) 119–123.